

Rethinking annotation granularity for overcoming deep shortcut learning:

A retrospective study on chest radiographs

Luyang Luo^{1*}, Hao Chen^{2*}, Yongjie Xiao³, Yanning Zhou¹,

Xi Wang¹, Varut Vardhanabhuti⁴, Mingxiang Wu⁵ & Pheng-Ann Heng^{1,6*}

ABSTRACT

Deep learning has demonstrated radiograph screening performances that are comparable or superior to radiologists. However, recent studies show that deep models for thoracic disease classification usually show degraded performance when applied to external data. Such phenomena can be categorized into shortcut learning, where the deep models learn unintended decision rules that can fit the identically distributed training and test set but fail to generalize to other distributions. A natural way to alleviate this defect is explicitly indicating the lesions and focusing the model on learning the intended features. In this paper, we conduct extensive retrospective experiments to compare a popular thoracic disease classification model, CheXNet, and a thoracic lesion detection model, CheXDet. We first showed that the two models achieved similar image-level classification performance on the internal test set with no significant differences under many scenarios. Meanwhile, we found incorporating external training data even led to performance degradation for CheXNet. Then, we compared the models' internal performance on the lesion localization task and showed that CheXDet achieved significantly better performance than CheXNet even when given 80% less training data. By further visualizing the models' decision-making regions, we revealed that CheXNet learned patterns other than the target lesions, demonstrating its shortcut learning defect. Moreover, CheXDet achieved significantly better external performance than CheXNet on both the image-level classification task and the lesion localization task. Our findings suggest improving annotation granularity for training deep learning systems as a promising way to elevate future deep learning-based diagnosis systems for clinical usage.

¹ Department of Computer Science and Engineering, The Chinese University of Hong Kong, Hong Kong, China.

² Department of Computer Science and Engineering, The Hong Kong University of Science and Technology, Hong Kong, China.

³ AI Research Lab, Imsight Technology, Co., Ltd., Shenzhen, China.

⁴ Department of Diagnostic Radiology, Li Ka Shing Faculty of Medicine, The University of Hong Kong, Hong Kong, China.

⁵ Department of Radiology, Shenzhen People's Hospital, Luohu, Shenzhen, China.

⁶ Guangdong-Hong Kong-Macao Joint Laboratory of Human-Machine Intelligence-Synergy Systems, Shenzhen Institutes of Advanced Technology, Chinese Academy of Sciences, China.

*email: lyluo@cse.cuhk.edu.hk; jhc@cse.ust.hk; pheng@cse.cuhk.edu.hk

INTRODUCTION

Deep learning (DL)¹ has demonstrated remarkable performance in analyzing medical images for computer-aided diagnosis (CAD)², where expert-level performances have been reported on various tasks³⁻¹². As a type of data-driven approach, DL-based CAD systems require large amounts of supervision signals, which is expertise-demand, time-consuming, and hard to obtain for medical images¹³. Therefore, medical images often cannot be comprehensively annotated by medical experts¹⁴. Large-scale datasets like Chest X-ray (CXR) often leverage natural language processing (NLP) algorithms to mine the image-level labels from radiological reports¹⁵⁻¹⁹. Hence, massive studies develop DL models that perform CXR screening by predicting whether different kinds of abnormalities exist from the whole radiograph level, i.e., classification models^{12,20-26}.

Despite the high accuracies achieved on many thoracic diseases, studies have shown that DL models tend to make decisions out of wrong reasons²⁷⁻²⁹ and demonstrated significantly degraded performances when applied to external testing^{26,27}. For example, by visualizing the class activating maps³⁰, researchers found that a DL model leveraged hospital metal tokens on the chest radiographs instead of lesion patterns as the supporting regions to make decisions^{27,28}. Recent studies refer to such phenomena as shortcut learning³¹, where the deep neural networks learn unintended patterns to fit the training data quickly. These unintended patterns are often highly co-occurred with the target classes and easier to be recognized than factors causing the diseases (e.g., salient patterns such as hospital tokens). While the classification models are only trained to output “1” for diseased cases and “0” for non-diseased ones, the spurious correlations can be easily selected for decision making^{29,32}. In other words, the DL-based classification models can be prone to being right for the wrong reasons³³. Moreover, machine learning studies broadly hypothesize that the training and testing sets are independent and identically distributed (i.i.d.). Therefore, using the co-occurrence or correlations contribute largely to the drastically degraded external performance, where the external dataset is out of the training set’s distribution, and the correlations are also missing.

A natural thought to alleviate the shortcut learning defect is incorporating more training data to cover a larger distribution. Meanwhile, some studies also proposed restricting the DL models to focus on diseased regions with finer-grained annotations^{30,34}. For instance, Li et al.³⁵ found the DL model attended to “water” when classifying an image to the class “boat.” To rectifying this learned pattern from the correlations, they took advantage of a small amount of box-level or pixel-level annotations and managed to guide the DL model’s visual cues onto the target objects. Succeeding studies further enabled more explicit attention rectification with human interaction by actively specifying the target regions of interests^{28,36}. Specifically, in thoracic diseases screening from CXR images, some works have demonstrated increasing classification accuracy using a small number of bounding boxes that locate lesions^{23,37,38}. Meanwhile, researchers have also developed successful thoracic lesion detection models using finer-grained annotations^{8,25,39}. Thus far, both DL-based classification model^{9,12,16} and detection model^{8,25} have been reported to achieve comparable or even superior performance to

practicing radiologists. Although high screening accuracies are achieved, many studies were limited to proposing novel models to improve internal performances, and previous works had not thoroughly analyzed the efficacy of the two types of deep neural networks. When and how different granularities of annotations benefit DL models for CXR diagnosis remained an open question yet to be answered.

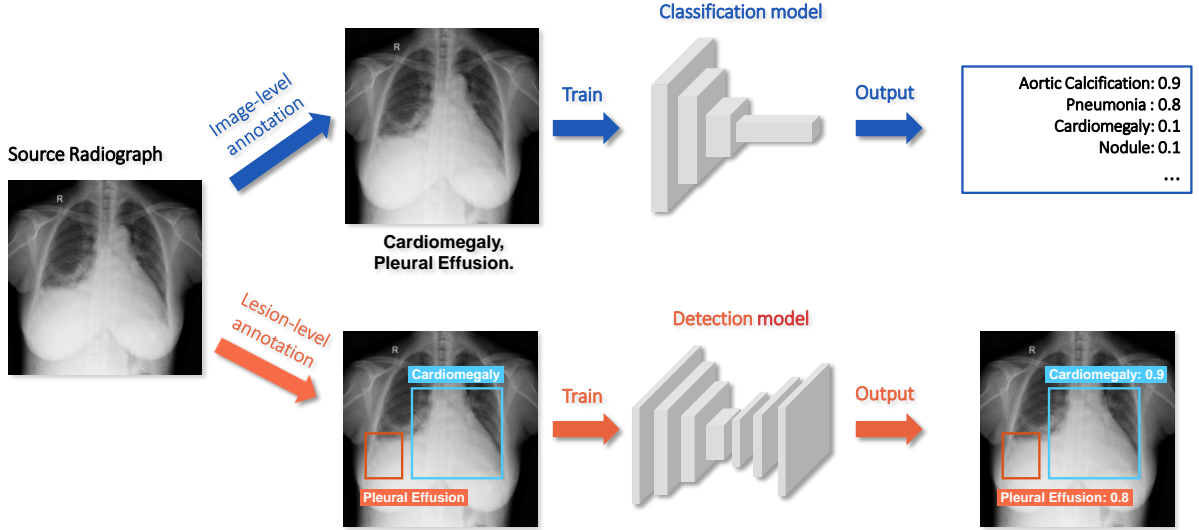


Fig. 1 Training flows comparison between classification model and detection model. Image-level annotations only indicate whether specific diseases exist on the whole radiograph, while lesion-level annotations further point out the exact locations of lesions with bounding boxes. As a result, the classification model only predicts the probabilities of each pathology's existence, while the detection model could identify the lesion regions with corresponding disease scores.

In this paper, we argue that the fundamental question for improving medical image diagnosis lies in finer-grained annotations, not fancier models, when available data are abundant. To this end, we extensively investigated the above questions by thoroughly comparing a classification model, CheXNet⁹, and a detection model we developed, called CheXDet, under various scenarios. A comparison of the two types of models is illustrated in Figure 1. Specifically, 34,501 radiographs from 30,561 patients were collected from multiple China hospitals and labeled with nine common cardiothoracic diseases. The cohort was split into a training set for algorithm development, a validation set for model selection, and a hold-out set for performance assessment. We trained CheXNet with radiograph-level annotations and trained CheXDet with lesion-level bounding boxes. Both models could predict the disease's existence, while CheXDet was further required to locate specific lesions. We evaluated both models on the internal testing set as well as three radiologist-labeled open-access validation datasets, NIH-Google²¹, PadChest¹⁸, and ChestX-ray14¹⁵.

Results show that: 1) different granularities of annotations lead to comparable internal performances for radiograph-level classification; 2) incorporating additional data does not

benefit CheXNet's performance; 3) both models achieved comparable performance to practicing radiologists on the internal set; 4) CheXDet showed significantly better lesion detection performances, while CheXNet learned unintended patterns for decision-making; and 5) CheXDet achieved significantly better external performance on both classification and detection tasks, indicating finer-grained annotations could alleviate the shortcut learning phenomenon and help the chest X-ray screening model to be right for the right reasons.

RESULTS

Comparison of internal radiograph-level classification performance on Imsight Chest X-ray dataset (ImsightCXR)

We first compare the two models' radiograph-level classification performance, where both are only required to predict whether certain diseases exist in the whole CXR image. The majority votes of two radiologists and the radiological reports were used as the reference standard of "ground truth." We considered scenarios with different training data numbers, where we used 20%, 40%, 60%, 80%, or 100% data from our training set to develop CheXNet and CheXDet. We also trained a CheXNet model with 100% of our training data plus training data from the CheXpert dataset¹⁶. Supplementary Table 1 and Supplementary Table 2 show the specific number of radiographs and lesions in each split. Figure 2 illustrates the boxplots for AUCs with confidence intervals (CIs) of different models and the p-values of statistical tests under the five scenarios.

As shown in Figure 2, there were no statistically significant differences between the two models under most of the scenarios. However, when 20% training data was used, CheXNet and CheXDet showed significant differences in classifying fracture (p-value<0.05), pneumonia (p-value<0.01), pneumothorax (p-value<0.05), tuberculosis (p-value<0.05), and aortic calcification (p-value<0.001). When 40% or 100% training data were available, the two models also showed significant differences (p-values < 0.05) in classifying tuberculosis. Moreover, CheXNet trained on the combination of two datasets (100% ImsightCXR plus CheXPert) showed significantly poorer performance in classifying mass (p-value<0.05), nodule (p-value<0.001), tuberculosis (p-value<0.001), and aortic calcification (p-value<0.001) than those of CheXDet. Specific statistics of AUCs with CIs, sensitivities, and specificities of different models can be found in Supplementary Table 6.

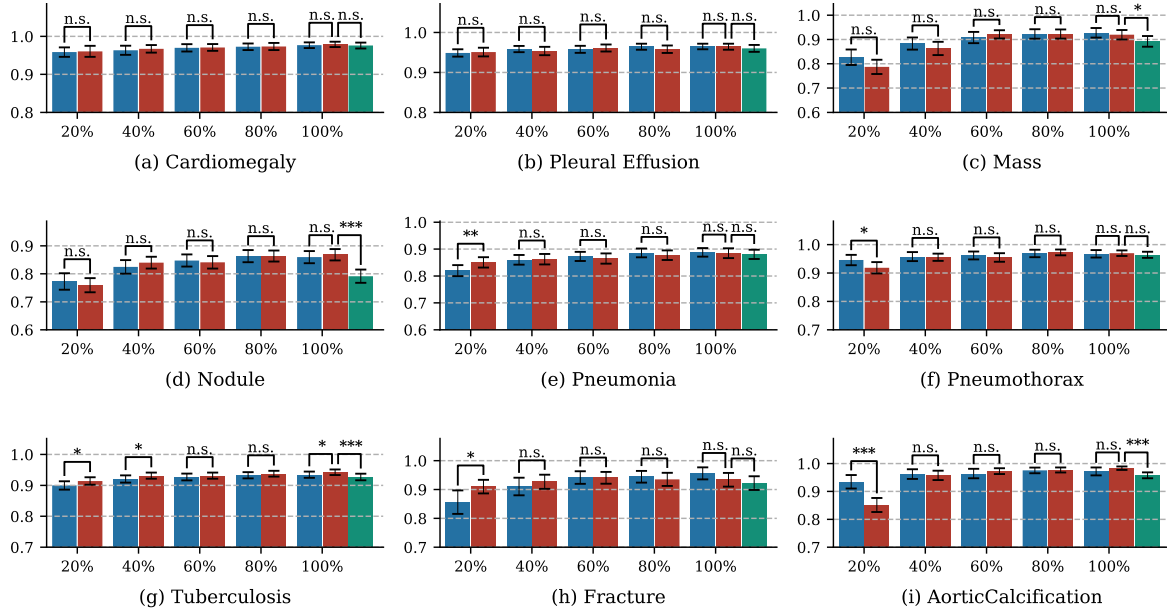


Fig. 2 Radiograph-level classification performance comparison of models on the internal testing set under different ratios of training data. Blue bars represent the area under the receiver operating characteristic curves (AUCs) with 95% confidence intervals (CIs) for CheXNet, red bars represent AUCs with 95% CIs for CheXDet, and green bars represent AUCs with 95% CIs for CheXNet trained with additional data from CheXpert dataset. Whiskers represent the CIs. n.s.: not significant. * $p < 0.05$. ** $p < 0.01$. *** $p < 0.001$.

Comparison of internal lesion-level localization performance on InsightCXR

We compared the lesion localization ability between the two models on our interval validation set. The lesion location reference standards were bounding boxes delineated by two radiologists and checked by one senior radiologist in case of disagreement. CheXDet directly predicted bounding boxes for possible lesions, while the bounding boxes predictions of CheXNet were extracted by Gradient-weighted Class Activation Mapping (Grad-CAM)³⁴, which is a widely adopted algorithm to extract localization information learned by the classification models^{9,40}.

Figure 3 illustrates the jackknife alternative free-response receiver-operating characteristic (JAFROC) figure of merits (FOMs) with CIs for CheXDet and CheXNet. Here, we compared CheXDet developed with 20%, 40%, 60%, 80%, and 100% training data against CheXNet trained with 100% data. Under all scenarios and other pathologies, CheXDet achieved significantly higher performance (p -values < 0.001) than CheXNet, even when developed with only 20% of training data. Meanwhile, the JAFROC-FOMs for each pathology of CheXDet increased continually with the increasing training data. The JAFROC-FOMs rose about 10% when the amount of training data increased from 20% to 100%. Specific statistics of JAFROC-FOMs with CIs of different models can be found in Supplementary Table 7.

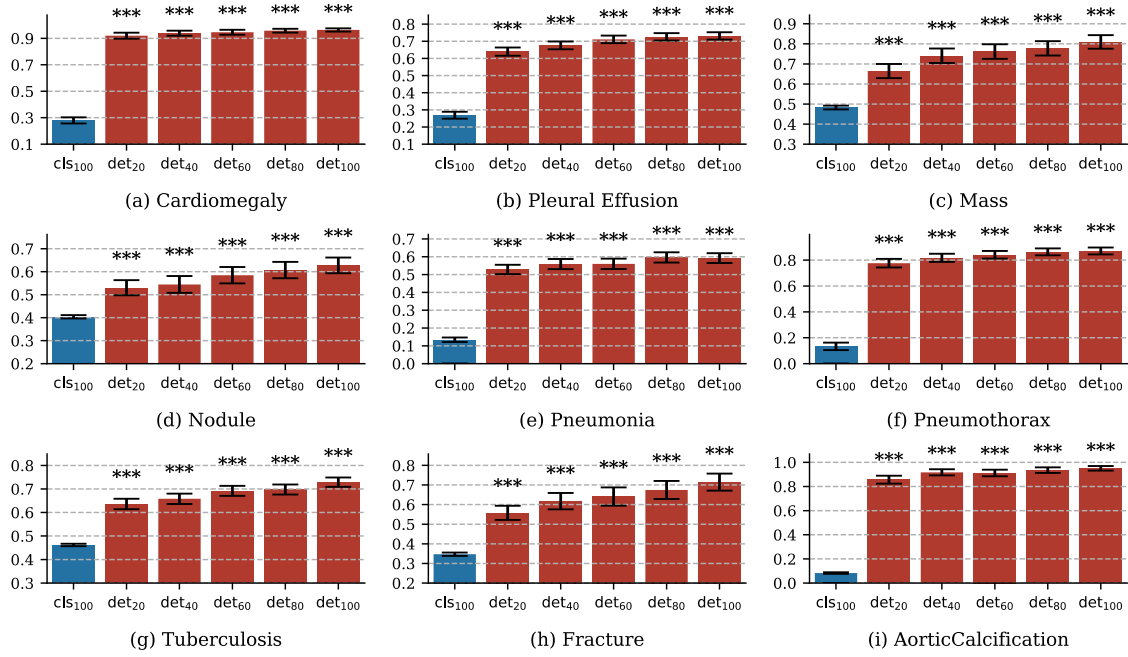


Fig. 3 Lesion-level localization performance comparison of models on the internal testing set. CheXNet developed with 100% data (cls₁₀₀) is compared against CheXDet developed with different ratios of data (det₂₀, det₄₀, det₆₀, det₈₀, and det₁₀₀; subscripts denote ratios of training data). Blue bars represent jackknife alternative free-response receiver-operating (JAFROC) figure of merits (FOMs) with 95% confidence intervals (CIs) of CheXNet, and red bars represent JAFROC-FOMs with 95% CIs of CheXDet. Whiskers represent the CIs. *** $p < 0.001$.

Comparison of external classification performance on NIH-Google dataset

We applied both models to the open-access NIH-Google dataset²¹. This external validation set contains 4,376 radiographs sampled from the NIH ChestX-ray14 dataset¹⁵ and re-annotated by at least three radiologists per image into four pathologies: fracture, mass or nodule, pneumothorax, and airspace opacity. Since opacity contains subcategories like atelectasis, edema, and infiltration, which were not labeled in our training set, we did not compare the models' performance in this class. Moreover, we take the maximum of the models' predictions on mass and nodule to be the probability for "mass or nodule." Here, we compared four different models: CheXNet developed with 100% training data (CheXNet₁₀₀), CheXNet developed with additional data from CheXPert (CheXNet₁₀₀₊), CheXDet developed with 20% training data (CheXDet₂₀), and CheXDet developed with 100% training data (CheXDet₁₀₀).

Table 1 reports the AUC with CIs for different models as well as p-values compared against CheXNet₁₀₀. On the one hand, CheXNet₁₀₀₊ showed significantly worse performance than CheXNet₁₀₀ on classifying nodule or mass (p -value <0.001) on this external set, whereas these two models' performance on pneumothorax and fracture showed no significant differences. On the other hand, CheXDet₂₀ and CheXDet₁₀₀ achieved significantly better performances than

CheXNet₁₀₀ on nodule or mass (p-values<0.001) and fracture (p-values<0.001), and CheXDet₁₀₀ further showed significantly higher AUC on classifying pneumothorax (p-value<0.05).

Table 1. Radiograph-level classification performance comparison between models on the external Google-NIH dataset.

	CheXNet ₁₀₀	CheXNet ₁₀₀₊		CheXDet ₂₀		CheXDet ₁₀₀	
	AUC (95% CI)	AUC (95% CI)	p-value	AUC (95% CI)	p-value	AUC (95% CI)	p-value
Nodule or Mass	0.6797 (0.6556, 0.7037)	0.6361 (0.6115, 0.6607)	< 0.001	0.7386 (0.7171, 0.7601)	< 0.001	0.7947 (0.7753, 0.8140)	< 0.001
Pneumothorax	0.8418 (0.8138, 0.8698)	0.8431 (0.8172, 0.8691)	0.9179	0.8224 (0.7953, 0.8494)	0.2199	0.8686 (0.8455, 0.8917)	0.0321
Fracture	0.5104 (0.4666, 0.5542)	0.5071 (0.4641, 0.5501)	0.8871	0.6615 (0.6226, 0.7004)	< 0.001	0.6728 (0.6327, 0.7129)	< 0.001

AUC: area under the receiver operating characteristic curve. CI: confidence interval. CheXNet₁₀₀: CheXNet developed with 100% ImsightCXR training data. CheXNet₁₀₀₊: CheXNet developed with 100% ImsightCXR training data plus additional data from CheXPert. CheXDet₂₀: CheXDet developed with 20% ImsightCXR training data. CheXDet₁₀₀: CheXDet developed with 100% ImsightCXR training data.

Comparison of external classification performance on PadChest dataset

We further evaluated the models on an external validation set from PadChest¹⁹. Specifically, we used 24,536 frontal view radiographs of which the labels were manually mapped from study reports onto Unified Medical Language System⁴¹ controlled biomedical vocabulary unique identifiers by trained physicians. This external testing set contains detailed radiograph-level labels, and we were able to evaluate the models' performances on all nine abnormalities. Here, we also compared the performances of CheXNet₁₀₀, CheXNet₁₀₀₊, CheXDet₂₀, and CheXDet₁₀₀.

Table 2 reports the AUCs with CIs for different models as well as p-values compared against CheXNet₁₀₀. CheXNet₁₀₀₊ showed significantly better performances on cardiomegaly (p-value<0.001), mass (p-value<0.001), and fracture (p-value<0.01) but significantly worse performances on nodule (p-value<0.001), pneumonia (p-value<0.01), and aortic calcification (p-value<0.001) than those of CheXNet₁₀₀. These two models did not have significant differences in pleural effusion, pneumothorax, and tuberculosis. Meanwhile, CheXDet₂₀ achieved significantly better performances than CheXNet₁₀₀ on mass (p-value<0.001), nodule

(p-value<0.001), and fracture (p-value<0.001), whereas significantly worse performances of CheXDet₂₀ were reported on cardiomegaly (p-value<0.001), pleural effusion (p-value<0.01), and aortic calcification (p-value<0.05). These two models did not show significant differences in pneumonia, pneumothorax, and tuberculosis. Regarding CheXDet₁₀₀, it showed significantly better performances than CheXNet₁₀₀ in mass (p-value<0.001), nodule (p-value<0.001), pneumonia (p-value<0.001), tuberculosis (p-value<0.05), and fracture (p-value<0.001), whereas worse performance was found on pleural effusion (p-value<0.05). These two models did not have significant differences in cardiomegaly, pneumothorax, and aortic calcification.

Table 2. Radiograph-level classification performance comparison between models on the external PadChest dataset.

	CheXNet ₁₀₀	CheXNet ₁₀₀₊		CheXDet ₂₀		CheXDet ₁₀₀	
	AUC (95% CI)	AUC (95% CI)	p-value	AUC (95% CI)	p-value	AUC (95% CI)	p-value
Cardiomegaly	0.9128 (0.9073, 0.9182)	0.9207 (0.9157, 0.9256)	<0.001	0.8841 (0.8767, 0.8915)	<0.001	0.9140 (0.9081, 0.9200)	0.6075
Pleural Effusion	0.9514 (0.9419, 0.9610)	0.9517 (0.9424, 0.9611)	0.9067	0.9409 (0.9317, 0.9501)	0.0038	0.9424 (0.9319, 0.9530)	0.0365
Mass	0.5505 (0.5280, 0.5730)	0.5893 (0.5679, 0.6108)	<0.001	0.6716 (0.6531, 0.6901)	<0.001	0.6325 (0.6119, 0.6532)	<0.001
Nodule	0.6566 (0.6280, 0.6852)	0.5542 (0.5266, 0.5817)	<0.001	0.7273 (0.7033, 0.7513)	<0.001	0.7780 (0.7545, 0.8016)	<0.001
Pneumonia	0.7910 (0.7739, 0.8081)	0.7710 (0.7553, 0.7867)	0.0013	0.8027 (0.7873, 0.8180)	0.0889	0.8265 (0.8123, 0.8408)	<0.001
Pneumothorax	0.8246 (0.7727, 0.8764)	0.8084 (0.7509, 0.8659)	0.5532	0.7818 (0.7094, 0.8543)	0.2233	0.8527 (0.7898, 0.9157)	0.3012
Tuberculosis	0.8910 (0.8566, 0.9254)	0.8796 (0.8449, 0.9142)	0.4689	0.9006 (0.8685, 0.9327)	0.4504	0.9216 (0.8903, 0.9529)	0.0419
Fracture	0.5504 (0.5283, 0.5725)	0.5824 (0.5604, 0.6043)	0.0074	0.7345 (0.7140, 0.7550)	<0.001	0.7828 (0.7621, 0.8035)	<0.001
Aortic Calcification	0.8629 (0.8521, 0.8737)	0.8049 (0.7928, 0.8171)	<0.001	0.8493 (0.8370, 0.8617)	0.0244	0.8711 (0.8600, 0.8823)	0.1077

AUC: area under the receiver operating characteristic curve. CI: confidence interval. CheXNet₁₀₀: CheXNet developed with 100% ImsightCXR training data. CheXNet₁₀₀₊: CheXNet developed with 100% ImsightCXR training data plus additional data from CheXPert. CheXDet₂₀: CheXDet developed with 20% ImsightCXR training data. CheXDet₁₀₀: CheXDet developed with 100%

ImsightCXR training data.

Comparison of external localization performance on NIH ChestX-ray14 dataset

We investigated the external lesion localization performance among the models on a subset with localization annotations from NIH ChestX-ray14¹⁵. This subset includes 983 images with eight different pathological lesions annotated by bounding boxes. Here, six pathologies overlapped with ImsightCXR were used in this experiment: cardiomegaly, effusion, nodule, mass, pneumonia, and pneumothorax.

Table 3 reports the JAFROC-FOMs with CIs for CheXNet₁₀₀, CheXDet₂₀, and CheXDet₁₀₀. We also conducted significance test between CheXNet₁₀₀ and the two detection models. CheXDet₁₀₀ achieved significantly higher performance on cardiomegaly, effusion, mass, pneumonia, and pneumothorax with JAFROC-FOMs of 0.7866 (95% CI 0.7461, 0.8272), 0.2588 (95% CI 0.2142, 0.3034), 0.5560 (95% CI 0.4800, 0.6320), 0.3349 (95% CI 0.2734, 0.3964), and 0.5454 (95% CI 0.4780, 0.6128), respectively, whereas CheXNet₁₀₀ achieved JAFROC-FOMs of 0.0842 (95% CI 0.0559, 0.1124), 0.1686 (95% CI 0.1202, 0.2170), 0.4517 (95% CI 0.4419, 0.4615), 0.1794 (95% CI 0.1429, 0.2158), and 0.0428 (95% CI 0.0075, 0.0780), respectively. There was no statistically significant difference on nodule. Moreover, CheXDet₂₀ trained with only 20% data also showed significant better performance than CheXNet₁₀₀ on cardiomegaly (p-values < 0.001), pleural effusion (p-values<0.01), pneumonia (p-values < 0.001), and pneumothorax (p-values < 0.001). There were no statistically significant differences of CheXDet₂₀ and CheXNet₁₀₀ on nodule and mass.

Table 3. Lesion-level localization performance comparison between models on the external NIH-ChestX-ray14 testing set.

	CheXNet ₁₀₀	CheXDet ₂₀		CheXDet ₁₀₀	
Pathology	JAFROC-FOM (95% CI)	JAFROC-FOM (95% CI)	p-value	JAFROC-FOM (95% CI)	p-value
Cardiomegaly	0.0842 (0.0559, 0.1124)	0.6494 (0.5980, 0.7008)	< 0.0001	0.7866 (0.7461, 0.8272)	< 0.0001
Effusion	0.1686 (0.1202, 0.2170)	0.2456 (0.2059, 0.2852)	< 0.01	0.2588 (0.2142, 0.3034)	< 0.01
Nodule	0.3099 (0.2909, 0.3289)	0.3097 (0.2457, 0.3736)	0.9944	0.3099 (0.2406, 0.3717)	0.9135
Mass	0.4517 (0.4419, 0.4615)	0.4036 (0.3451, 0.4620)	0.1096	0.5560 (0.4800, 0.6320)	0.0074
Pneumonia	0.1794 (0.1429, 0.2158)	0.3326 (0.2752, 0.3900)	< 0.0001	0.3349 (0.2734, 0.3964)	< 0.001

Pneumothorax	0.0428 (0.0075, 0.0780)	0.4049 (0.3432, 0.4666)	< 0.0001	0.5454 (0.4780, 0.6128)	< 0.0001
--------------	-------------------------	-------------------------	----------	-------------------------	----------

CheXNet trained with 100% data (CheXNet-100) is compared against CheXDet trained with 20% (CheXDet-20) and 100% data (CheXDet-100). JAFROC-FOM: free-response receiver-operating characteristic figure of merit. CI: confidence interval.

Comparison of deep learning models with radiologists on ImsightCXR

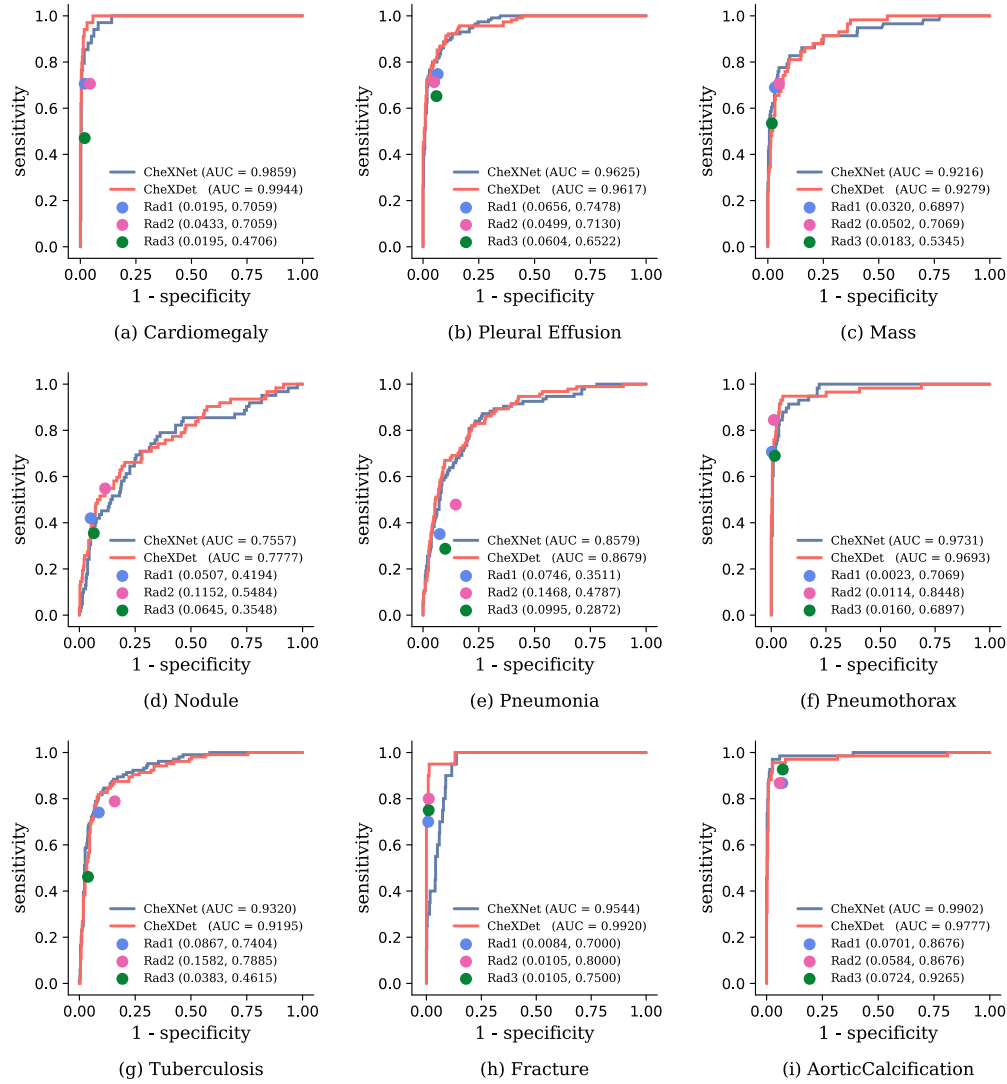


Fig. 4 Radiograph-level pathology classification performance comparison among models and radiologists on the testing subset. Blue curves represent AUCs of CheXNet. Red curves represent AUCs of CheXDet. Radiologists' performance levels are represented as single points. Radiologists 1, 2, and 3 have 13, 9, and 4 years of experience in radiology, respectively. Rad: radiologist. AUC: area under the receiver operating characteristic curve.

We further compared the performance of the models developed with 100% training data against practice radiologists. Three radiologists (with 4, 13, and 19 years of experience, respectively) were requested to individually read 496 randomly selected radiographs from our original testing set. Specific lesion delineations were requested if any pathology was found on the chest radiograph. A chest radiograph is considered with negative findings if no annotation is drawn. Sensitivities and specificities were evaluated per radiologist per disease.

Figure 4 illustrates the performance of all radiologists as well as the ROCs of the two models. Radiologists showed relatively high specificities (> 0.9) with a trade-off on sensitivities. Almost all the points representing individual radiologists lie on or under the ROC of one of the models, which means there exist thresholds where at least one model performs on par or better than practicing radiologists.

DISCUSSION

The recent decade has witnessed remarkable successes in deep learning, leading to a large number of applications to different medical tasks. As the most prevalent medical imaging technique globally, Chest X-ray also draws lots of attention from deep learning researchers. Many previous studies focused on improving DL-based CAD systems with better-designed algorithms^{22,28,38,42-45}. Some other works tried to use more training data from different institutions to improve the data-driven DL models^{21,26}. Despite the high AUC scores, study²⁷ showed that DL models might poorly generalize to data from external hospitals. Particularly, the DL models were reported to be good at using correlations such as hospital tokens²⁷ or patient variables²⁹ to predict diseases categorized in the phenomenon called shortcut learning³¹. Based on the findings from previous works, several questions remain not answered: does more data always lead to better DL CAD models? How significant do finer-grained annotations bring the improvement? More importantly, how is the generalization on the external data of different models? With our results, we answer these questions as follows.

We developed CheXNet and CheXDet, two models trained with different granularities of annotations, on our internal training set. We found that the two models showed no significant radiograph-level classification differences on the internal testing set under most of the scenarios. Further, we found that incorporating more training data from CheXPert could lead to performance drop on internal and external testing sets. This finding is in line with Zech et al.²⁷, whose findings showed incorporating multi-institutional data resulted in a performance drop. One possible reason is that the DL models could overfit the disease prevalence in the training set. Hence, during testing, the changing disease prevalence leads to degraded AUCs. Luo et al.²⁶ argued that the image appearance and label inconsistency differences are also the reasons. They developed better models and showed increasing AUCs when training with multi-institutional data. However, they also found performance became saturated when increasing training data from 300,000 images to 600,000 images. Combining these findings, we argue that although deep learning is data-driven, incorporating more training data does not always benefit the classification accuracy. Moreover, by comparing the two models to practicing radiologists, we found both models show comparable radiograph-level disease recognition performance to

the human experts. Many previous studies also reported the DL-based models achieving expert-level performances on automatic disease diagnosis. However, our analysis here shows that the metric used for comparing the DL models and humans could be ill-posed.

Essentially, performance on the testing data is one of the critical criteria to determine whether a CAD system can be applied to clinical usage. For radiograph-level classification, we conducted external testing on two datasets, NIH-Google²¹ and a subset of PadChest¹⁹, both hand-labeled by radiologists with sophisticated criteria. We found that although CheXNet and CheXDet did not show significant differences under most of the scenarios of the internal set, CheXDet mostly achieved significantly higher AUCs on these external data than CheXNet. Notably, on nodule, mass, and fracture, whose lesions could be very small, CheXDet performed significantly better than CheXNet on both datasets, even when developed with 20% of the training data. When both developed by 100% training data, CheXDet significantly outperformed CheXNet for all diseases except for cardiomegaly, pleural effusion, and aortic calcification on PadChest. However, the two models' absolute AUC values are relatively high and close on the mentioned three diseases. Importantly, these findings show that DL models developed with finer-grained annotations are more generalizable to the external data, which holds more promising potential for clinical usages.

As mentioned, DL models could favor shortcut learning. Here, we compared the lesion localization performances of the two types of models on both the internal set and the external ChestX-ray14 dataset¹⁵. Following previous works, we also utilized Grad-CAM³⁴ for CheXNet to indicate lesion locations. Not surprisingly, CheXNet showed significantly worse lesion localization performance than CheXDet. The primary reason is that CheXDet is trained by bounding box annotations. One may also argue that CheXNet is not trained to identify multiple lesions from the radiograph, and the gradient maps usually show the most discriminative regions for recognizing objects³⁰. However, the CXR images we used from ChestX-ray14 contain a single lesion for each disease at most, while CheXNet performed significantly worse than CheXDet on localizing most of the diseases. These findings altogether indicate that CheXNet cannot locate lesions well.

Furthermore, failing to find the lesions suggests that CheXNet makes decisions from image patterns other than the pathological regions. We further visualize the localization results of the two models in Figure 5. It can be observed that CheXNet's attention is not exactly on the intended lesions (Figure 5 a, b, and d) and sometimes even on false regions (Figure 5 c). Again, our finding demonstrates that the DL model trained with radiograph-level annotations used hospital tokens or other unintended patterns for decision-making. The poor lesion localization performance and external classification performance of CheXNet, together with the visualization results, show that a DL model trained with radiograph-level annotations is prone to shortcut learning. On the contrary, a DL model trained with finer-annotations, e.g., bounding boxes, is more robust to external data and less prone to shortcut learning by correctly attending to the correct pathological patterns. Hence, our findings suggest that the fundamental question for applying current DL models to clinical usage does not entirely lie in the data or the model

but the annotations as well, which is underappreciated in the existing literature.

Our work could be further improved. First, a few of the available public datasets are hand-labeled by radiologists. Hence, we choose NIH-Google, PadChest, and ChestX-ray14 to be the external testing sets. As a result, some external validation datasets did not obtain the same pathology categories as our internal set. Therefore, we could only test on the classes overlapping with our annotations at the current stage. Second, based on recent studies⁴⁶, correctly localizing the lesion does not necessarily mean the shortcut learning is fully addressed. As can be observed from our findings, the external performance of CheXDet is not as good as its internal performance. As generalization performance drop often reveals shortcut learning³¹, we suppose that CheXDet also conducts shortcut learning but less prone than CheXNet. The possible reasons might be that CheXDet overfits the disease prevalence on the internal set or makes the decision out of only one attribute of the lesion, e.g., the texture⁴⁷. Our study poses an open question: how can we finally know that a DL-based medical model makes the right decision out of the right reasons? One possible solution is including human interactions to attribute the data and actively correcting the model’s recognition^{36,48,49}. Finally, as bounding box annotations are scarce and image-level annotations can be easily acquired, it is also essential to develop annotation-efficient models that possess good lesion localization performance with fewer lesion annotations.

To summarize, we validate that a deep learning model trained with image-level annotations is prone to shortcut learning that utilizes unintended patterns for decision-making for disease screening from CXR images. By comprehensively comparing CheXDet against CheXNet, we argue that fine-grained annotations are essential to overcome the performance degradation brought by shortcut learning. Our findings suggest future studies should develop deep medical models that make the right predictions for the right reasons towards more robust and correct disease classification.

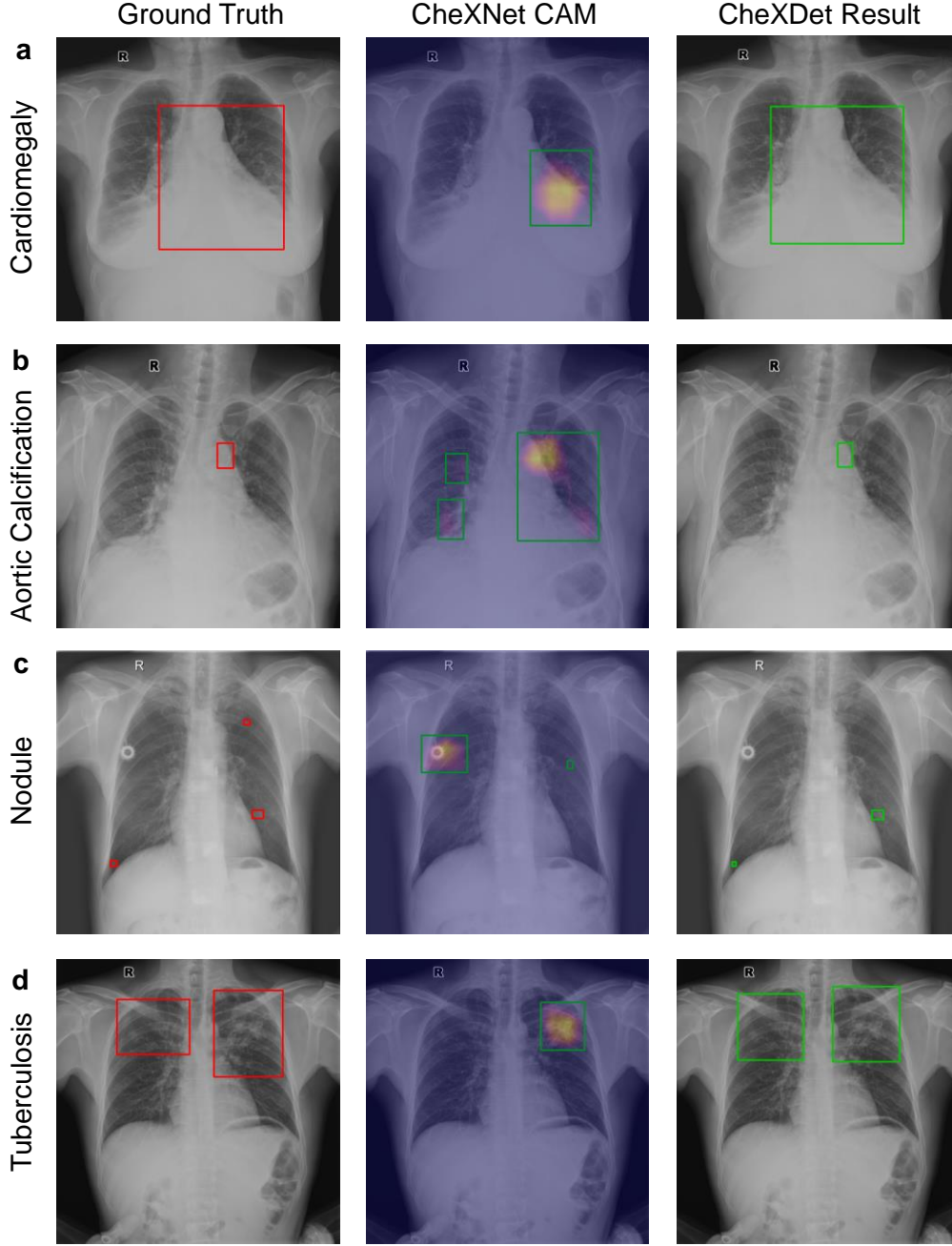


Fig. 5 **Localization results of CheXNet and CheXDet.** The left, middle, and right panels illustrate ground truth bounding boxes, class activating map generated by CheXNet, and localization output of CheXDet, respectively. a: CheXDet output correct bounding box for cardiomegaly, while CheXNet only focuses on the left heart region. b: CheXDet output correct bounding box for aortic calcification, while CheXNet generates a larger region of interest and false positives on the right lung. c: CheXDet detects correct fracture lesion, while CheXNet focuses on false positives and artifacts. d: CheXDet successfully detects multiple nodule lesions, while CheXNet generates large regions of interest with false positives. CAM: class activating map.

METHODS

Ethics approval

Internal data (ImsightCXR dataset) construction and analysis were approved by The Medical Ethical Committee of Shenzhen People's Hospital. Requirement for individual patient consent was waived by the committee because the study was retrospective and did not affect clinical diagnosis. All external data are publically available, of which the approval for analysis was waived.

Internal Dataset Construction

We retrospectively collected 34,501 frontal view radiographs and their corresponding text reports of 30,561 patients from the clinical PACS system at three Chinese hospitals. All involved radiological studies were conducted from 2005 to 2019. The patients included 16,959 males, 11,458 females, and 2144 where gender was unknown. Patients' ages were 48.5 ± 18.6 . We split the data into three different sets for training (28,673 radiographs from 25,019 patients), validation (2,906 radiographs from 2,751 patients), and testing (2,922 radiographs from 2,791 patients). We further split the training set into five subsets with approximate equal size to obtain 20% (5,763 radiographs from 5,421 patients), 40% (11,493 radiographs from 10,594 patients), 60% (17,180 radiographs from 15,527 patients), and 80% (22,943 radiographs from 20,336 patients) training data. To compare the performance of models against radiologists, we randomly sampled a subset with 496 radiographs from the testing set. This dataset is referred to as Imsight Chest X-ray dataset (ImsightCXR). Detailed numbers of each split's pathologies and lesions can be found in Supplementary Table 1 and Supplementary Table 2.

External Datasets

To compare the robustness of the two models, we further studied two external datasets: 1. National Institutes of Health (NIH) Database: two subsets were used from this database: (a) A subset from NIH "ChestX-ray14" dataset hand-labeled by Google Health²¹: a total of 4,376 frontal chest radiographs from the original ChestX-ray14 database¹⁵ were re-labeled with at least three radiologists per image. Fracture, mass or nodule, opacity, and pneumothorax were annotated. Since our internal dataset did not have enough samples of subcategories of opacity, such as atelectasis, we leveraged the other three pathologies annotations in our study. Detailed numbers of radiographs for each pathology can be found in Supplementary Table 3. (b) A subset from NIH "ChestX-ray14" dataset with 984 radiographs was used. This subset contains eight diseases with 200 bounding box annotations hand-labeled by a board-certified radiologist. We studied six diseases (cardiomegaly, effusion, nodule, mass, pneumonia, and pneumothorax) that our models were trained to recognize. Detailed numbers of images and bounding boxes for each pathology can be found in Supplementary Table 5. 2. PadChest dataset: A subset of 24,536 frontal radiographs from the original PadChest database¹⁸ was used. The text reports of these samples were automatically labeled and manually reviewed by trained physicians. The PadChest dataset contains about two hundred labels, and all pathologies we used to train the models could be found in this database. Detailed numbers of patients for each pathology can

be found in Supplementary Table 4.

Classification Model Development

We trained CheXNet using the same convolutional neural network architecture, i.e., a 121-layer DenseNet⁵⁰, as same as Rajpurkar et al.⁹, except that we required the model to output probabilities for nine pathologies. The model parameters were transferred from a DenseNet-121 pre-trained on the ImageNet Large Scale Visual Recognition Challenge database⁵¹ with about 1.3 million natural images of 1000 object classes. We replaced the original final output layer (1000-way softmax) of the pre-trained network with nine neurons with the sigmoid function that outputs the disease probabilities. Regarding the model developed from InsightCXR and CheXPert, the number of output neurons is 16, which is the union of the pathologies of two datasets. We resized radiographs to 512×512 for both training and testing. During training, we randomly flipped the input images horizontally to enrich the training data (known as data augmentation). We set the training objective as minimizing the average per-class cross-entropy between the model’s prediction and ground truth (0 or 1 indicates absence or presence of specific pathology). We used Adam⁵² as the optimization solver with an initial learning rate of 0.001. We also adopted a cosine decay strategy that repeatedly set the learning rate to the initial value and gradually decrease it. We input 48 radiographs to the network for each model updating step until the whole training set had been fed to the model 25 times (25 epochs). After each epoch on the validation set, we evaluated the model and chose the one with the best AUCs for later-on experiments on the testing set. The models were trained on 4 TITAN XP GPUs with 12 GB of memory each. The implementations were done using the PyTorch (<https://pytorch.org>) deep learning framework.

Detection Model Development

We developed CheXDet following the framework of EfficientDet⁵³. The model was required to predict proposals of possible lesion regions as well as the corresponding pathology probabilities. The feature extractor backbone, EfficientNet⁵⁴, was a convolutional neural network initially designed by the neural network architecture search technique on ImageNet. The backbone down-sampled the input gradually to 1/32 with a scale of two, which could be divided into seven stages accordingly. We leveraged the features generated at the last layers of stages 2, 3, 4, and 5 to find possible pathologies' region-of-interests. Specifically, these features were fed into a weighted bi-directional feature pyramid network, a.k.a., BiFPN, which introduced rich cross-scale connections to the multi-scale features. We then fed the outputs of BiFPN into a region proposal network⁵⁵ (RPN) to densely predict whether a proposal box is a foreground (i.e., lesions) or background (i.e., healthy tissues). The proposals with the highest foreground scores would be further fed into two lightweight convolutional networks to predict their specific pathology categories and bounding-box locations. The details of the network and specific components are described in referred papers.

We initialized CheXDet with the pre-trained weights of EfficientDet from ImageNet and reset the output size of the classification net to be nine classes. We resized each radiograph to

768×768 for both training and testing. We also randomly flipped the input images horizontally to enrich the training data. We set the training objective as minimizing the summation of the cross-entropy of each region proposals and a smooth L1 loss for regressing coordinates of the bounding boxes. We used Stochastic Gradient Descent with an initial learning rate of 0.005 to be the optimizer. We fed each time three images to the network and trained the model for 120,000 steps. The learning rate was decayed twice with a ratio of 0.1 at steps 70,000 and 100,000, respectively. We evaluated the model every 5000 steps and chose the one with the best lesion-level accuracy for later-on experiments on the testing set. The models were trained on one TITAN XP GPU with 12 GB memory. During testing, we required the model to generate 100 bounding-boxes with corresponding pathology probabilities. The implementations were done using the Detectron2 (<https://github.com/facebookresearch/detectron2>) package based on PyTorch (<https://pytorch.org>) framework.

Reader Study

For each radiograph in Insight Chest X-ray dataset (InsightCXR), two readers were assigned from a cohort of ten radiologists (range of experience, 4-30 years in general radiology). They were provided with corresponding text reports to label mentioned pathological findings and bounding boxes of the lesions. If both radiologists disagreed with the report, their consensus with the radiological reports would be taken as the ground truth. For lesion bounding box annotations, if two readers disagree with each other, another senior radiologist (at least 20 year-experience) from the cohort would be involved to make the final decision. These readers were not further involved in comparison with the models. The three radiologists that compared with the models had 4, 13, and 19 years of experience, respectively. All readers were provided with an online graphical user interface (GUI)-based annotation infrastructure. The radiographs were available to authorized persons only. All images were of the same size as their original digital imaging and communications in medicine (DICOM) format. Other information in the DICOM was not provided. The readers could zoom in and out using the software and change the intensity contrast of the images, and images were viewed using monitors with resolution equivalent to that used in clinical reporting. They made binary decisions on the available frontal view radiographs, blinded to the radiology text reports and other readers' annotations. All readers were provided with the same guidelines to the annotation software and rules.

Quantification and statistical analysis

The comparisons of pathology identification and lesion localization were conducted both in-between models as well as between models and practicing radiologists. The classification evaluation criteria for models were the area under the receiver-operating characteristic (AUC) with a 95% confidence interval (CI). We used DeLong test⁵⁶ to compute the CI and p-values between ROCs. The lesion localization criterion for models was weighted alternative free-response receiver operating characteristics (wAFROC) as the figures of merit (FOMs) by jackknife AFROC (JAFROC) (version 4.2.1; <https://github.com/dpc10ster/WindowsJafroc>). We performed a 95% CI computation and significance test for JAFROC-FOMs with a paired t-test, applying the Dorfman-Berbaum-Metz model with the fixed-case, random-reader method.

For classification models, we used gradient-guided class activation mapping³⁴, i.e., Grad-CAM, to generate heatmaps, on which higher intensities (resp. warmer color) indicate higher probabilities of suspicious lesions. We set a threshold of 0.6 on the normalized heatmap to determine the lesion-level existence and eliminated the values lower than the threshold. We generated bounding boxes on the remained connected components. For CheXDet, we directly used the bounding-boxed predictions. The bounding box was regarded as a true positive proposal if the intersection-over-union (IoU) with a ground truth bounding-box is greater than 0.5. To measure the pathology identification performance for radiologists, we computed radiograph-level sensitivity and specificity. All the measurements and statistical analyses were done using the free software R language (<https://www.r-project.org>).

DATA AVAILABILITY

Data from NIH-Google were acquired from <https://www.kaggle.com/nih-chest-xrays/data>, and the annotations of NIH-Google were acquired from https://cloud.google.com/healthcare/docs/resources/public-datasets/nih-chest#additional_labels. Data and annotations of PadChest were obtained from <http://bimcv.cipf.es/bimcv-projects/padchest>. Data and annotations of NIH-ChestX-ray14 were obtained from <https://www.kaggle.com/nih-chest-xrays/data>. Data from InsightCXR are not publicly available due to reasonable privacy and security concerns.

CODE AVAILABILITY

The source code used in this study can be available upon request from the corresponding authors (L. L., H. C., or P. A.H.).

ACKNOWLEDGEMENTS

This work was supported by Key-Area Research and Development Program of Guangdong Province, China (2020B010165004), Hong Kong Innovation and Technology Fund (Project No. ITS/311/18FP and Project No. ITS/426/17FP), and National Natural Science Foundation of China with Project No. U1813204.

AUTHOR CONTRIBUTIONS

L. L. and H. C. conceived the work. L. L. and Y. X. carried out experiments and analysis. L. L. drafted the paper, and all authors contributed to the writing and revision of the paper.

COMPETING INTERESTS

The authors declare no competing interests.

ADDITIONAL INFORMATION

Correspondance and requests for materials should be addressed to L. L., H. C., or P. A.H.

1. LeCun, Y., Bengio, Y. & Hinton, G. Deep learning. *nature* **521**, 436-444 (2015).
2. Topol, E.J. High-performance medicine: the convergence of human and artificial intelligence. *Nature medicine* **25**, 44-56 (2019).
3. Bejnordi, B.E., *et al.* Diagnostic assessment of deep learning algorithms for detection of lymph node metastases in women with breast cancer. *Jama* **318**, 2199-2210 (2017).
4. De Fauw, J., *et al.* Clinically applicable deep learning for diagnosis and referral in retinal disease. *Nature medicine* **24**, 1342-1350 (2018).
5. Lin, L., *et al.* Deep learning for automated contouring of primary tumor volumes by MRI for nasopharyngeal carcinoma. *Radiology* **291**, 677-686 (2019).
6. Liu, Y., *et al.* A deep learning system for differential diagnosis of skin diseases. *Nature Medicine*, 1-9 (2020).
7. Monteiro, M., *et al.* Multiclass semantic segmentation and quantification of traumatic brain injury lesions on head CT using deep learning: an algorithm development and multicentre validation study. *The Lancet Digital Health* (2020).
8. Nam, J.G., *et al.* Development and validation of deep learning-based automatic detection algorithm for malignant pulmonary nodules on chest radiographs. *Radiology* **290**, 218-228 (2019).
9. Rajpurkar, P., *et al.* Deep learning for chest radiograph diagnosis: A retrospective comparison of the CheXNeXt algorithm to practicing radiologists. *PLoS medicine* **15**, e1002686 (2018).
10. Ran, A.R., *et al.* Detection of glaucomatous optic neuropathy with spectral-domain optical coherence tomography: a retrospective training and validation deep-learning analysis. *The Lancet Digital Health* **1**, e172-e182 (2019).
11. Setio, A.A.A., *et al.* Validation, comparison, and combination of algorithms for automatic detection of pulmonary nodules in computed tomography images: the LUNA16 challenge. *Medical image analysis* **42**, 1-13 (2017).
12. Tang, Y.-X., *et al.* Automated abnormality classification of chest radiographs using deep convolutional neural networks. *NPJ Digital Medicine* **3**, 1-8 (2020).
13. Litjens, G., *et al.* A survey on deep learning in medical image analysis. *Medical image analysis* **42**, 60-88 (2017).
14. Tajbakhsh, N., *et al.* Embracing imperfect datasets: A review of deep learning solutions for medical image segmentation. *Medical Image Analysis* **63**, 101693 (2020).
15. Wang, X., *et al.* Chestx-ray8: Hospital-scale chest x-ray database and benchmarks on weakly-supervised classification and localization of common thorax diseases. in *Proceedings of the IEEE conference on computer vision and pattern recognition* 2097-2106 (2017).
16. Irvin, J., *et al.* Chexpert: A large chest radiograph dataset with uncertainty labels and expert comparison. in *Proceedings of the AAAI Conference on Artificial Intelligence*, Vol. 33 590-597 (2019).
17. Johnson, A.E., *et al.* MIMIC-CXR, a de-identified publicly available database of chest radiographs with free-text reports. *Scientific Data* **6**(2019).

18. Bustos, A., Pertusa, A., Salinas, J.-M. & de la Iglesia-Vayá, M. Padchest: A large chest x-ray image dataset with multi-label annotated reports. *Medical Image Analysis*, 101797 (2020).
19. Bustos, A., Pertusa, A., Salinas, J.-M. & de la Iglesia-Vayá, M. Padchest: A large chest x-ray image dataset with multi-label annotated reports. *Medical image analysis* **66**, 101797 (2020).
20. Dunnmon, J.A., *et al.* Assessment of convolutional neural networks for automated classification of chest radiographs. *Radiology* **290**, 537–544 (2019).
21. Majkowska, A., *et al.* Chest radiograph interpretation with deep learning models: assessment with radiologist-adjudicated reference standards and population-adjusted evaluation. *Radiology* **294**, 421–431 (2020).
22. Wang, H., Jia, H., Lu, L. & Xia, Y. Thorax-Net: An Attention Regularized Deep Neural Network for Classification of Thoracic Diseases on Chest Radiography. *IEEE journal of biomedical and health informatics* **24**, 475–485 (2019).
23. Guan, Q., *et al.* Discriminative Feature Learning for Thorax Disease Classification in Chest X-ray Images. *IEEE Transactions on Image Processing* **30**, 2476–2487 (2021).
24. Chen, H., Miao, S., Xu, D., Hager, G.D. & Harrison, A.P. Deep hierarchical multi-label classification applied to chest X-ray abnormality taxonomies. *Medical image analysis* **66**, 101811 (2020).
25. Hwang, E.J., *et al.* Development and validation of a deep learning-based automated detection algorithm for major thoracic diseases on chest radiographs. *JAMA network open* **2**, e191095–e191095 (2019).
26. Luo, L., *et al.* Deep mining external imperfect data for chest X-ray disease screening. *IEEE Transactions on Medical Imaging* **39**, 3583–3594 (2020).
27. Zech, J.R., *et al.* Variable generalization performance of a deep learning model to detect pneumonia in chest radiographs: a cross-sectional study. *PLoS medicine* **15**, e1002683 (2018).
28. Huang, Y.-J., *et al.* Rectifying Supporting Regions with Mixed and Active Supervision for Rib Fracture Recognition. *IEEE Transactions on Medical Imaging* (2020).
29. Badgeley, M.A., *et al.* Deep learning predicts hip fracture using confounding patient and healthcare variables. *NPJ digital medicine* **2**, 1–10 (2019).
30. Zhou, B., Khosla, A., Lapedriza, A., Oliva, A. & Torralba, A. Learning deep features for discriminative localization. in *Proceedings of the IEEE conference on computer vision and pattern recognition* 2921–2929 (2016).
31. Geirhos, R., *et al.* Shortcut learning in deep neural networks. *Nature Machine Intelligence* **2**, 665–673 %@ 2522–5839 (2020).
32. Castro, D.C., Walker, I. & Glocker, B. Causality matters in medical imaging. *Nature Communications* **11**, 1–10 (2020).
33. Lapuschkin, S., *et al.* Unmasking clever hans predictors and assessing what machines really learn. *Nature communications* **10**, 1–8 (2019).
34. Selvaraju, R.R., *et al.* Grad-cam: Visual explanations from deep networks via gradient-based localization. in *Proceedings of the IEEE international conference on*

- computer vision* 618–626 (2017).
35. Li, K., Wu, Z., Peng, K.-C., Ernst, J. & Fu, Y. Guided attention inference network. *IEEE transactions on pattern analysis and machine intelligence* (2019).
 36. Schramowski, P., *et al.* Making deep neural networks right for the right scientific reasons by interacting with their explanations. *Nature Machine Intelligence* **2**, 476–486 (2020).
 37. Liu, J., *et al.* Align, attend and locate: Chest x-ray diagnosis via contrast induced attention network with limited supervision. in *Proceedings of the IEEE/CVF International Conference on Computer Vision* 10632–10641 (2019).
 38. Li, Z., *et al.* Thoracic disease identification and localization with limited supervision. in *Proceedings of the IEEE Conference on Computer Vision and Pattern Recognition* 8290–8299 (2018).
 39. Liu, Y., Wu, Y.-H., Ban, Y., Wang, H. & Cheng, M.-M. Rethinking computer-aided tuberculosis diagnosis. in *Proceedings of the IEEE/CVF Conference on Computer Vision and Pattern Recognition* 2646–2655 (2020).
 40. Zhou, J., *et al.* Weakly supervised 3D deep learning for breast cancer classification and localization of the lesions in MR images. *Journal of Magnetic Resonance Imaging* **50**, 1144–1151 (2019).
 41. Bodenreider, O. The unified medical language system (UMLS): integrating biomedical terminology. *Nucleic Acids Res.* **32**, D267–D270 (2004).
 42. Zhou, Y., *et al.* Contrast-Attentive Thoracic Disease Recognition with Dual-Weighting Graph Reasoning. *IEEE Transactions on Medical Imaging* (2021).
 43. Ouyang, X., *et al.* Learning Hierarchical Attention for Weakly-supervised Chest X-Ray Abnormality Localization and Diagnosis. *IEEE Transactions on Medical Imaging* (2020).
 44. Chen, B., Li, J., Lu, G., Yu, H. & Zhang, D. Label Co-occurrence Learning with Graph Convolutional Networks for Multi-label Chest X-ray Image Classification. *IEEE Journal of Biomedical and Health Informatics* (2020).
 45. Wang, X., Peng, Y., Lu, L., Lu, Z. & Summers, R.M. Tienet: Text-image embedding network for common thorax disease classification and reporting in chest x-rays. 9049–9058 (2018).
 46. Viviano, J.D., Simpson, B., Dutil, F., Bengio, Y. & Cohen, J.P. Saliency is a Possible Red Herring When Diagnosing Poor Generalization. in *International Conference on Learning Representations* (2021).
 47. Geirhos, R., *et al.* ImageNet-trained CNNs are biased towards texture; increasing shape bias improves accuracy and robustness. in *International Conference on Learning Representations* (2019).
 48. Stammer, W., Schramowski, P. & Kersting, K. Right for the Right Concept: Revising Neuro-Symbolic Concepts by Interacting with their Explanations. in *Proceedings of the IEEE conference on computer vision and pattern recognition* (2021).
 49. Oakden-Rayner, L., Dunnmon, J., Carneiro, G. & Ré, C. Hidden stratification causes clinically meaningful failures in machine learning for medical imaging. in *Proceedings of the ACM conference on health, inference, and learning* 151–159 (2020).

50. Huang, G., Liu, Z., Van Der Maaten, L. & Weinberger, K.Q. Densely connected convolutional networks. in *Proceedings of the IEEE conference on computer vision and pattern recognition* 4700–4708 (2017).
51. Deng, J., *et al.* Imagenet: A large-scale hierarchical image database. in *2009 IEEE conference on computer vision and pattern recognition* 248–255 (Ieee, 2009).
52. Kingma, D.P. & Ba, J. Adam: A method for stochastic optimization. in *International Conference on Learning Representations* (2015).
53. Tan, M., Pang, R. & Le, Q.V. Efficientdet: Scalable and efficient object detection. in *Proceedings of the IEEE/CVF Conference on Computer Vision and Pattern Recognition* 10781–10790 (2020).
54. Tan, M. & Le, Q. EfficientNet: Rethinking Model Scaling for Convolutional Neural Networks. in *International Conference on Machine Learning* 6105–6114 (2019).
55. Ren, S., He, K., Girshick, R. & Sun, J. Faster r-cnn: Towards real-time object detection with region proposal networks. in *Advances in neural information processing systems* 91–99 (2015).
56. Sun, X. & Xu, W. Fast implementation of DeLong’ s algorithm for comparing the areas under correlated receiver operating characteristic curves. *IEEE Signal Processing Letters* **21**, 1389–1393 (2014).

SUPPLEMENTARY INFORMATION

Supplementary Table 1. Numbers of radiographs for each pathology in each internal dataset.

<div>Dataset</div> <div>Pathology</div>	testing	validation	train/100%	train/80%	train/60%	train/40%	train/20%
Aortic Calcification	191	171	1705	1394	1019	686	372
Cardiomegaly	207	195	2068	1695	1270	798	425
Effusion	449	420	4112	3260	2441	1671	819
Fracture	129	146	1324	1060	809	515	251
Mass	221	221	624	494	360	264	134
Nodule	348	355	3412	2740	2027	1385	713
Pneumonia	444	433	4256	3431	2581	1675	850
Pneumothorax	242	228	2289	1836	1394	895	442
Tuberculosis	772	773	8154	6546	4907	3247	1639

Supplementary Table 2. Numbers of lesions for each pathology in each internal dataset.

<div> Dataset Pathology </div>	testing	validation	train/100%	train/80%	train/60%	train/40%	train/20%
Aortic Calcification	193	173	1767	1445	1055	712	390
Cardiomegaly	207	195	2068	1695	1270	798	425
Effusion	562	532	5118	4069	3047	2071	1022
Fracture	364	329	3524	2796	2087	1437	709
Mass	251	243	675	540	396	279	144
Nodule	592	508	5183	4099	3053	2132	1046
Pneumonia	620	623	6007	4816	3625	2382	1191
Pneumothorax	270	253	2535	2029	1544	991	485
Tuberculosis	1238	1243	12978	10416	7770	5208	2646

Supplementary Table 3. Number of images in the external Google-NIH test dataset

Pathology	Images
Fracture	186
Pneumothorax	238
Nodule or mass	605

Supplementary Table 4. Number of images in the external PadChest test dataset

Pathology	Images
Cardiomegaly	2205
Effusion	672
Fracture	679
Mass	791
Nodule	474
Pneumonia	935
Pneumothorax	63
Tuberculosis	126
Aortic Calcification	999

Supplementary Table 5. Numbers of images and lesions for each pathology in the external ChestX-ray14 test dataset.

Pathology	Images	Lesions
Cardiomegaly	146	146
Effusion	153	153
Mass	85	85
Nodule	79	79
Pneumonia	120	120
Pneumothorax	95	95

Supplementary Table 6. Specific AUCs, sensitivities and specificities of CheXNet and CheXDet on InsightCXR. The

cutting points for sensitivities and specificities are computed from validation set.

		CheXNet			CheXDet		
Pathology	Ratio of training data	AUC	Sensitivity	Specificity	AUC	Sensitivity	Specificity
Cardiomegal y	20%	0.9606 (0.9462, 0.9751)	0.9179 (0.8696, 0.9565)	0.9101 (0.8442, 0.9348)	0.9586 (0.9461, 0.9711)	0.9179 (0.8744, 0.9565)	0.8910 (0.7959, 0.9160)
	40%	0.9672 (0.9573, 0.9771)	0.8937 (0.8454, 0.9420)	0.9267 (0.8807, 0.9462)	0.9634 (0.9513, 0.9754)	0.9275 (0.8792, 0.9614)	0.8796 (0.8273, 0.9083)
	60%	0.9708 (0.9619, 0.9798)	0.9469 (0.9130, 0.9758)	0.8956 (0.7227, 0.9245)	0.9699 (0.9602, 0.9795)	0.9275 (0.8841, 0.9614)	0.9127 (0.8475, 0.9426)
	80%	0.9734 (0.9640, 0.9828)	0.9565 (0.9179, 0.9807)	0.8766 (0.7403, 0.9042)	0.9727 (0.9640, 0.9814)	0.9179 (0.8744, 0.9565)	0.9241 (0.8829, 0.9510)

	100%	0.9790 (0.9721, 0.9859)	0.9469 (0.9082, 0.9758)	0.9050 (0.8460, 0.9337)	0.9768 (0.9694, 0.9842)	0.9420 (0.9082, 0.9758)	0.9179 (0.8615, 0.9378)
	100% + CheXpert	0.9759 (0.9682, 0.9837)	0.9565 (0.9227, 0.9807)	0.9017 (0.7981, 0.9297)	N/A	N/A	N/A
Effusion	20%	0.9509 (0.9401, 0.9617)	0.9087 (0.8753, 0.9354)	0.8609 (0.8176, 0.8872)	0.9487 (0.9394, 0.9580)	0.8931 (0.8597, 0.9243)	0.8746 (0.8374, 0.9022)
	40%	0.9536 (0.9430, 0.9642)	0.8953 (0.8597, 0.9243)	0.8884 (0.8471, 0.9098)	0.9585 (0.9508, 0.9663)	0.9176 (0.8886, 0.9465)	0.8536 (0.8221, 0.8807)
	60%	0.9611 (0.9523, 0.9700)	0.8953 (0.8641, 0.9265)	0.9030 (0.8633, 0.9276)	0.9577 (0.9489, 0.9666)	0.8797 (0.8441, 0.9087)	0.9013 (0.8585, 0.9264)
	80%	0.9581 (0.9487, 0.9674)	0.9109 (0.8797, 0.9376)	0.8848 (0.8492, 0.9090)	0.9642 (0.9567, 0.9717)	0.8864 (0.8508, 0.9176)	0.9098 (0.8722, 0.9373)

	100%	0.9644 (0.9569, 0.9718)	0.8886 (0.8530, 0.9198)	0.8981 (0.8641, 0.9252)	0.9649 (0.9579, 0.9719)	0.8731 (0.8396, 0.9042)	0.9143 (0.8775, 0.9402)
	100% + CheXpert	0.9601 (0.9514, 0.9687)	0.8842 (0.8486, 0.9131)	0.9046 (0.8726, 0.9329)	N/A	N/A	N/A
Fracture	20%	0.9101 (0.8865, 0.9336)	0.8760 (0.8140, 0.9380)	0.7773 (0.6681, 0.8400)	0.8563 (0.8156, 0.8970)	0.7132 (0.6357, 0.7907)	0.8779 (0.7490, 0.9277)
	40%	0.9269 (0.9024, 0.9514)	0.8217 (0.7519, 0.8837)	0.8786 (0.7974, 0.9348)	0.9106 (0.8801, 0.9411)	0.8605 (0.7829, 0.9147)	0.8235 (0.6656, 0.8865)
	60%	0.9406 (0.9202, 0.9610)	0.8915 (0.8295, 0.9380)	0.8761 (0.7139, 0.9116)	0.9415 (0.9197, 0.9633)	0.8295 (0.7674, 0.8915)	0.9037 (0.8174, 0.9485)
	80%	0.9353 (0.9125, 0.9581)	0.7829 (0.7054, 0.8527)	0.9391 (0.8560, 0.9638)	0.9444 (0.9240, 0.9647)	0.8295 (0.7597, 0.8915)	0.9245 (0.7798, 0.9628)

	100%	0.9339 (0.9101, 0.9578)	0.8760 (0.8062, 0.9380)	0.8815 (0.7279, 0.9026)	0.9560 (0.9351, 0.9769)	0.9070 (0.8450, 0.9535)	0.8912 (0.8185, 0.9284)
	100% + CheXpert	0.9223 (0.8985, 0.9461)	0.8605 (0.7829 0.9147)	0.8314 (0.7537, 0.8912)	N/A	N/A	N/A
Mass	20%	0.7873 (0.7579, 0.8168)	0.8462 (0.7919, 0.8959)	0.6035 (0.5050, 0.6546)	0.8269 (0.7949, 0.8589)	0.6199 (0.5520, 0.6833)	0.8776 (0.7986, 0.9230)
	40%	0.8632 (0.8358, 0.8906)	0.6833 (0.6154, 0.7421)	0.8893 (0.8156, 0.9234)	0.8833 (0.8583, 0.9083)	0.7240 (0.6606, 0.7828)	0.8912 (0.8256, 0.9289)
	60%	0.9212 (0.9041, 0.9383)	0.8869 (0.8416, 0.9321)	0.8008 (0.7340, 0.8453)	0.9081 (0.8847, 0.9314)	0.8507 (0.7963, 0.9005)	0.8286 (0.7208, 0.8801)
	80%	0.9225 (0.9038, 0.9412)	0.8145 (0.7555, 0.8643)	0.8830 (0.7869, 0.9082)	0.9226 (0.9031, 0.9421)	0.8507 (0.7964, 0.8959)	0.8384 (0.7582, 0.8937)

	100%	0.9196 (0.9002, 0.9390)	0.8235 (0.7692, 0.8733)	0.8571 (0.8027, 0.8982)	0.9275 (0.9079, 0.9471)	0.8462 (0.7919, 0.8914)	0.8697 (0.8086, 0.9008)
	100% + CheXpert	0.8922 (0.8701, 0.9143)	0.7557 (0.7014, 0.8145)	0.8517 (0.7771, 0.8964)	N/A	N/A	N/A
Nodule	20%	0.7592 (0.7339, 0.7846)	0.8362 (0.7931, 0.8793)	0.5447 (0.4615, 0.5890)	0.7726 (0.7432, 0.8021)	0.6178 (0.5603, 0.6695)	0.8147 (0.7343, 0.8524)
	40%	0.8400 (0.8190, 0.8611)	0.7615 (0.7155, 0.8075)	0.7545 (0.6954, 0.7964)	0.8247 (0.8004, 0.8490)	0.7960 (0.7471, 0.8420)	0.7380 (0.6402, 0.7758)
	60%	0.8411 (0.8189, 0.8634)	0.7759 (0.7241, 0.8190)	0.7564 (0.7059, 0.7920)	0.8477 (0.8258, 0.8695)	0.7414 (0.6925, 0.7874)	0.7873 (0.7323, 0.8353)
	80%	0.8636 (0.8440, 0.8832)	0.6897 (0.6408, 0.7385)	0.8508 (0.7933, 0.8877)	0.8630 (0.8413, 0.8847)	0.7644 (0.7183, 0.8075)	0.8190 (0.7622, 0.8644)

	100%	0.8681 (0.8479, 0.8883)	0.8075 (0.7586, 0.8506)	0.7580 (0.6993, 0.7968)	0.8597 (0.8380, 0.8814)	0.7356 (0.6868, 0.7845)	0.8221 (0.7669, 0.8586)
	100% + CheXpert	0.7915 (0.7677, 0.8152)	0.7328 (0.6810, 0.7787)	0.7265 (0.6570, 0.7646)	N/A	N/A	N/A
Pneumonia	20%	0.8507 (0.8313, 0.8701)	0.7342 (0.6892, 0.7770)	0.7881 (0.7389, 0.8285)	0.8200 (0.7995, 0.8406)	0.7883 (0.7387, 0.8333)	0.7022 (0.6513, 0.7341)
	40%	0.8626 (0.8432, 0.8820)	0.7815 (0.7342, 0.8221)	0.7910 (0.7349, 0.8341)	0.8602 (0.8420, 0.8784)	0.7748 (0.7297, 0.8176)	0.7805 (0.7377, 0.8180)
	60%	0.8651 (0.8460, 0.8841)	0.7793 (0.7365, 0.8198)	0.7930 (0.7357, 0.8337)	0.8728 (0.8557, 0.8900)	0.7995 (0.7545, 0.8401)	0.7692 (0.7211, 0.8043)
	80%	0.8773 (0.8596, 0.8951)	0.7995 (0.7545, 0.8379)	0.7974 (0.7333, 0.8301)	0.8860 (0.8697, 0.9022)	0.7320 (0.6869, 0.7748)	0.8676 (0.8204, 0.8975)

	100%	0.8848 (0.8667, 0.9029)	0.8266 (0.7860, 0.8671)	0.8075 (0.7566, 0.8394)	0.8880 (0.8719, 0.9041)	0.8356 (0.7928, 0.8739)	0.7756 (0.7135, 0.8043)
	100% + CheXpert	0.8804 (0.8634, 0.8976)	0.7860 (0.7410, 0.8266)	0.8025 (0.7446, 0.8350)	N/A	N/A	N/A
Pneumothorax	20%	0.9184 (0.8983, 0.9384)	0.8140 (0.7603, 0.8595)	0.9022 (0.8377, 0.9302)	0.9456 (0.9274, 0.9639)	0.8554 (0.8057, 0.9008)	0.9313 (0.8824, 0.9560)
	40%	0.9556 (0.9429, 0.9683)	0.8884 (0.8429, 0.9298)	0.8929 (0.8265, 0.9209)	0.9577 (0.9420, 0.9735)	0.8884 (0.8430, 0.9298)	0.9343 (0.8687, 0.9638)
	60%	0.9545 (0.9394, 0.9696)	0.8802 (0.8306, 0.9215)	0.9134 (0.8672, 0.9496)	0.9617 (0.9478, 0.9755)	0.9008 (0.8595, 0.9421)	0.9138 (0.8033, 0.9440)
	80%	0.9724 (0.9622, 0.9826)	0.9215 (0.8843, 0.9545)	0.9347 (0.8754, 0.9530)	0.9688 (0.9558, 0.9819)	0.9174 (0.8719, 0.9545)	0.9414 (0.8981, 0.9642)

	100%	0.9696 (0.9597, 0.9795)	0.9132 (0.8719, 0.9504)	0.9095 (0.8425, 0.9437)	0.9675 (0.9544, 0.9806)	0.9174 (0.8802, 0.9504)	0.9272 (0.8433, 0.9567)
	100% + CheXpert	0.9640 (0.9531, 0.9750)	0.9215 (0.8802, 0.9545)	0.8713 (0.8332, 0.9071)	N/A	N/A	N/A
Tuberculosis	20%	0.9141 (0.9021, 0.9261)	0.7979 (0.7591, 0.8278)	0.8893 (0.8498, 0.9088)	0.8999 (0.8864, 0.9134)	0.8174 (0.7850, 0.8472)	0.8458 (0.8107, 0.8730)
	40%	0.9316 (0.9217, 0.9415)	0.8692 (0.8342, 0.8977)	0.8540 (0.8163, 0.8772)	0.9207 (0.9089, 0.9325)	0.8666 (0.8329, 0.8964)	0.8335 (0.8042, 0.8595)
	60%	0.9315 (0.9217, 0.9414)	0.8141 (0.7811, 0.8446)	0.8916 (0.8595, 0.9144)	0.9274 (0.9164, 0.9383)	0.8886 (0.8562, 0.9158)	0.8219 (0.7809, 0.8460)
	80%	0.9379 (0.9286, 0.9473)	0.8983 (0.8705, 0.9210)	0.8381 (0.7995, 0.8647)	0.9327 (0.9225, 0.9429)	0.8718 (0.8368, 0.8990)	0.8614 (0.8270, 0.8833)

	100%	0.9426 (0.9336, 0.9516)	0.8575 (0.8303, 0.8821)	0.8800 (0.8479, 0.9098)	0.9346 (0.9245, 0.9448)	0.8744 (0.8433, 0.9028)	0.8605 (0.8321, 0.8865)
	100% + CheXpert	0.9272 (0.9165, 0.9378)	0.8523 (0.8232, 0.8782)	0.8586 (0.8144, 0.8851)	N/A	N/A	N/A
Aortic Calcification	20%	0.8515 (0.8263, 0.8766)	0.9110 (0.8639, 0.9476)	0.6613 (0.4939, 0.7023)	0.9346 (0.9105, 0.9587)	0.8796 (0.8272, 0.9267)	0.8934 (0.7389, 0.9323)
	40%	0.9576 (0.9407, 0.9744)	0.8482 (0.7906, 0.9005)	0.9506 (0.8799, 0.9722)	0.9623 (0.9449, 0.9796)	0.9267 (0.8691, 0.9686)	0.9271 (0.7433, 0.9425)
	60%	0.9727 (0.9624, 0.9830)	0.8901 (0.8377, 0.9319)	0.9473 (0.8887, 0.9685)	0.9641 (0.9472, 0.9811)	0.9215 (0.8743, 0.9581)	0.9410 (0.7580, 0.9627)
	80%	0.9769 (0.9678, 0.9860)	0.9372 (0.8953, 0.9686)	0.9081 (0.8700, 0.9440)	0.9754 (0.9653, 0.9856)	0.9372 (0.8953, 0.9686)	0.9315 (0.8151, 0.9550)

	100%	0.9833 (0.9770, 0.9897)	0.9319 (0.8848, 0.9634)	0.9546 (0.8810, 0.9692)	0.9718 (0.9574, 0.9861)	0.9529 (0.9110, 0.9843)	0.9218 (0.7375, 0.9539)
	100% + CheXpert	0.9578 (0.9471, 0.9685)	0.9319 (0.8796, 0.9634)	0.8594 (0.7737, 0.8923)	N/A	N/A	N/A

Supplementary Table 7. Specific statistics of JAFROC-FOMs of CheXNet and CheXDet on InsightCXR.

Pathology	CheXNet ₁₀₀ JAFROC-FOM	The ratio of training data for CheXDet	CheXDet JAFROC-FOM
Aortic Calcification	0.0832 (0.0764-0.0899)	20%	0.8565 (0.8237, 0.8892)
		40%	0.9173 (0.8918, 0.9428)
		60%	0.9119 (0.8847, 0.9391)
		80%	0.9352 (0.9121, 0.9582)
		100%	0.9506 (0.9318, 0.9693)
Cardiomegaly	0.2795 (0.2564-0.3026)	20%	0.9202 (0.8977, 0.9428)
		40%	0.9391 (0.9202, 0.9581)
		60%	0.9462 (0.9275, 0.9649)
		80%	0.9577 (0.9435, 0.9720)
		100%	0.9634 (0.9512, 0.9757)
Effusion	0.2688 (0.2488-0.2888)	20%	0.6398 (0.6157, 0.6639)
		40%	0.6762 (0.6532, 0.6992)
		60%	0.7111 (0.6890, 0.7331)
		80%	0.7265 (0.7050, 0.7479)

		100%	0.7315 (0.7100, 0.7529)
Fracture	0.3470 (0.3387-0.3554)	20%	0.5581 (0.5220, 0.5942)
		40%	0.6175 (0.5757, 0.6594)
		60%	0.6411 (0.5947, 0.6875)
		80%	0.6748 (0.6288, 0.7208)
		100%	0.7148 (0.6715, 0.7580)
Mass	0.4828 (0.4733-0.4922)	20%	0.6646 (0.6292, 0.7000)
		40%	0.7411 (0.7050, 0.7772)
		60%	0.7616 (0.7251, 0.7981)
		80%	0.7776 (0.7418, 0.8134)
		100%	0.8095 (0.7756, 0.8435)
Nodule	0.4038 (0.3966-0.4109)	20%	0.5304 (0.4976, 0.5632)
		40%	0.5446 (0.5080, 0.5813)
		60%	0.5847 (0.5491, 0.6203)
		80%	0.6072 (0.5716, 0.6427)
		100%	0.6276 (0.5935, 0.6618)

Pneumonia	0.1337 (0.1207-0.1467)	20%	0.5286 (0.5025, 0.5547)
		40%	0.5590 (0.5308, 0.5873)
		60%	0.5600 (0.5309, 0.5891)
		80%	0.5960 (0.5674, 0.6246)
		100%	0.5925 (0.5648, 0.6202)
Pneumothorax	0.1335 (0.1044-0.1627)	20%	0.7766 (0.7436, 0.8096)
		40%	0.8183 (0.7868, 0.8498)
		60%	0.8414 (0.8122, 0.8707)
		80%	0.8637 (0.8370, 0.8904)
		100%	0.8711 (0.8441, 0.8980)
Tuberculosis	0.4620 (0.4567-0.4672)	20%	0.6359 (0.6137, 0.6580)
		40%	0.6582 (0.6363, 0.6802)
		60%	0.6921 (0.6708, 0.7133)
		80%	0.6974 (0.6762, 0.7186)
		100%	0.7287 (0.7089, 0.7486)